AGU Advances

Supporting Information for

High-resolution Precipitation Monitoring with a Dense Seismic Nodal Array

J. Hua[1], M. Wu[2], J. P. Mulholland[3], J. D. Neelin[4], V. C. Tsai[5], D. T. Trugman[6]

[1] Department of Geological Sciences, Jackson School of Geosciences, The University of Texas at Austin; Austin, TX, 78712 USA.

[2] Joint Institute for Regional Earth System Science and Engineering, University of California, Los Angeles, Los Angeles, CA, 90095 USA.

[3] Department of Atmospheric Sciences, John D. Odegard School of Aerospace Sciences, The University of North Dakota, Grand Forks, ND, 58202 USA.

[4] Department of Atmospheric and Oceanic Sciences, University of California, Los Angeles, Los Angeles, CA, 90095 USA.

[5] Department of Earth, Environmental and Planetary Sciences, Brown University, Providence, RI, 02912 USA.

[6] Nevada Seismological Laboratory, University of Nevada, Reno, Reno, NV, 89557 USA.

Contents of this file

Additional Supporting Information (Files uploaded separately)

Introduction

This file contains the supplementary details for how the raindrop size distribution would affect seismic intensity; how we calculated the seismic PSD and removed anthropogenic noises; how the relative Earth structure response for each station was removed; how we combined seismic PSDs from individual stations to form a precipitation map; and how we empirically converted seismic PSDs to precipitation rates. This file also includes supplementary figures and tables for the article. Captions for the supplementary movies which are uploaded as separate .mp4 files are also included here.

Text S1. Ground for the consideration of raindrop size distribution

Generalized from the exponential distribution in the early study (Marshall & Palmer, 1948), the raindrop size distribution (DSD) is often parameterized as a normalized Gamma distribution (Testud et al., 2001):

$$N(D) = \frac{N_0}{D_0}\left(\frac{D}{D_0}\right)^{\mu} e^{-(\mu+4)\frac{D}{D_0}}, \tag{S1}$$

where D is the droplet equivolume spherical diameter, and N_0, D_0 and μ are all constants. Among them, N_0 characterizes the number of raindrops; D_0 characterizes the average size of raindrops; and μ controls the shape of the DSD. An example of this DSD is shown in Figure S5a, and eq. (S1) can well fit the observation. We assume all droplets have reached their terminal fall speed, and this fall speed only depends on the droplet size (D) and some known constants. One formulation (Gunn & Kinzer, 1949) involves the density of liquid water and air (ρ_w and ρ_a), and a dimensionless drag coefficient (c), and the square of the fall speed, v^2, is proportional to D:

$$v^2 = \frac{4}{3} gD \frac{\rho_w - \rho_a}{\rho_a c}, \tag{S2}$$

where g is the gravitational acceleration. Some other formulations also have a polynomial relationship between v and D (Rogers, 1989; Yau & Rogers, 1996), but one can show they will result in similar conclusions. In this case, similar to Bakker et al. (2022) the droplet average $|NF^2|$ appearing in eq. (2) should be written as an integral with respect to the spherical diameter :

$$\left|NF^2\right| = \int_0^{\infty} N(D) m^2(D) v^2(D) dD. \tag{S3}$$

Let the mass of raindrops be:

$$m = \frac{1}{6}\pi\rho_w D^3 \tag{S4}$$

then, combining eq. (S3) and eq. (S4) with eq. (S2):

$$\left|NF^2\right| = \left(\frac{1}{6}\pi\rho_w\right)^2 \cdot \frac{4}{3} g \frac{\rho_w - \rho_a}{\rho_a c} \frac{\Gamma(\mu+8)}{(\mu+4)^{\mu+8}} N_0 D_0^2 = \frac{\Gamma(\mu+8)}{(\mu+4)^{\mu+8}} N_0 m_0^2 v_0^2, \tag{S5}$$

where Γ is the gamma function, and m_0 and v_0 are the mass and the fall speed of a droplet of the size D_0, respectively. Similarly, the precipitation rate is characterized by:

$$PR = \frac{1}{\rho_w}\int_0^\infty N(D) m(D) dD = \frac{\Gamma(\mu+4)}{\rho_w(\mu+4)^{\mu+4}} N_0 m_0, \tag{S6}$$

and the average raindrop kinetic energy would be:

$$E = \frac{\int_0^\infty N(D)\frac{1}{2} m(D) v^2(D) dD}{\int_0^\infty N(D) dD} = \frac{\Gamma(\mu+5)}{2(\mu+4)^4\Gamma(\mu+1)} m_0 v_0^2. \tag{S7}$$

Therefore, combining eq. (S6) and eq. (S7) with eq. (S5), we obtain:

$$\left|NF^2\right| = \frac{\Gamma(\mu+8)\Gamma(\mu+1)}{\Gamma(\mu+5)\Gamma(\mu+4)} 2\rho_w \cdot PR \cdot E. \tag{S8}$$

This relationship suggests that the seismic PSD is directly dependent on the precipitation rate and raindrop kinetic energy.

Since eq. (S8) shows the PSD is also dependent on the shape of the DSD (μ), we examined its potential influence based on raindrop sizes recorded by an impact disdrometer located ~30 km away. Between Apr 2016 and Nov 2021, for any day with precipitation accumulation over 2 mm, we first fit observed DSD with eq. (S1) by solving for the unknown parameters, μ, N_0, and D_0 (e.g., Figure S5a). This optimization is done by expressing eq. (S1) in log-scale,

$$\log N = \mu \log D - \frac{\mu+4}{D_0} D + \left[\log N_0 - (\mu+1) D_0\right]. \tag{S9}$$

Hence, we could estimate the parameters we need from a bivariate (log$D$ and D) linear regression using the ordinary least square method to get the three parameters, and the slope for log$D$ is the shape parameter μ. The majority of optimized μ for the 257 precipitation days spans from 0.5 to 3 (Figure S5a).

We then evaluate the potential influence of varying μ on the seismic PSD. With the disdrometer providing $N(D)$, $m(D)$ and $v(D)$, the average raindrop kinetic energy (E) is calculated based on the first half of eq. (S7). Similarly, we also quantified $|NF^2|$ and PR (eq. S3 & S6), so that the PSD-PR difference can be directly estimated based on disdrometer observed data. The observed PSD-PR difference is then compared with both the observed average raindrop kinetic energy and μ (Figure S5b). We found though μ could influence this difference (eq. S8), it highly correlates with E instead of μ, which suggests the potential to retrieve raindrop kinetic energy from the PSD-PR difference.

Meanwhile, the parameter μ does not need to vary much in order to fit the observed DSD. As shown in Figure S5a, an example of the observed DSD could be successfully characterized when specifying different values of μ. In addition, the overall relationship between E and the PSD-PR difference in Figure S5b could be well reproduced using a constant μ of 2. We also systematically evaluate the coefficient of determination for fitting (r^2) for all 257 days, in the contexts of optimized or prescribed μ (Figure S5c). We found though the highest r^2 is achieved when μ is optimized, r^2 can still be high using a constant μ of 2, with 63% of r^2 over 0.98 and 90% of r^2 over 0.95 (Figure S5a). This finding further substantiates our treatment of the seismic PSD as a function of the precipitation rate and the raindrop kinetic energy.

Text S2. Seismic power spectral density calculation and noise removal

To calculate seismic power spectral densities, we used the Welch method (Welch, 1967). In this method, at every second, we extract seismic records that are ±5 s around it. This 10 s section is then divided into 200 windows, each with a length of 0.1s and overlaps the neighboring window by 50%. For each window, the PSD is calculated for 10-250 Hz, and the average of these 200 windows is used to represent the seismic PSD at the time. Therefore, the effective temporal resolution in this study is between 1 and 10 seconds. However, in practice, since precipitation signals mainly appears above 100 Hz, seismic PSD at 100-250 Hz could be confidently estimated as well using a 1 s section with 0.02 s long windows, which will bring a true 1 s temporal resolution.

With the calculated seismic PSD, anthropogenic noises were removed. During denoising, four frequency bands are used, the overall band 50-200 Hz ($PSD_{50\text{-}200}$); the first low frequency band 15-35 Hz ($PSD_{15\text{-}35}$); the second low frequency band 50-70 Hz ($PSD_{50\text{-}70}$); and the high frequency band 170-190 Hz ($PSD_{170\text{-}190}$). The overall band is used to identify strong pulses that are restricted in time. The two low frequency bands are similar to the two previously detected noise bands at 4-25 Hz (human activities) and 40-80 Hz (potentially related to thermoelastic and meteorological conditions) in Rindraharisaona et al. (2022), so are used here as characteristics to detect potential noises.

In practice, we first found all potential times for noise if one of the following 6 criteria is met: 1) $PSD_{50-200} \times PSD_{50-70} / PSD_{170-190}$ is over three times its root mean square for the whole event (rms); 2) $PSD_{50-200} \times PSD_{15-35} / PSD_{170-190}$ is over three times its rms; 3) $PSD_{50-200} / \mathrm{mean}_{100\mathrm{s}}(PSD_{50-200})$ is over three times its rms, where $\mathrm{mean}_{100\mathrm{s}}$ stands for taking the average *PSD* around ±50 s (a 100 s section); 4) $PSD_{50-200}^{2} / \mathrm{mean}_{100s}(PSD_{50-200})$ over three times its rms; 5) $\left[\mathrm{mean}_{10\mathrm{s}}(PSD_{50-200})\right]^{2} / \mathrm{mean}_{40\mathrm{s}}(PSD_{50-200})$ is over three times its rms; 6) $PSD_{50-200} / \mathrm{median}_{60\mathrm{s}}(PSD_{50-200})$ is over three times its rms, where $\mathrm{median}_{60\mathrm{s}}$ means the median *PSD* around ±30 s. Among them, the first two are designed to identify times with strong amplitudes at noise frequencies, and the other four are designed to identify short pulses with high amplitudes. With these potential times for noise, we obtained time windows that could contain them. For two neighboring windows, if the minimum $PSD_{50\text{-}200}$ in their interval is higher than one-third of the maximum $PSD_{50\text{-}200}$ of either window, the two windows are combined with their interval as one window. Then in each window, we searched beyond its two boundaries to find for the first time on either side that the $PSD_{50\text{-}200}$ is below one-third of the maximum $PSD_{50\text{-}200}$ within the window as the final boundaries of the window. If the maximum $PSD_{50\text{-}200}$ is over 10^{-16} m^2s^2, the window would be considered a noise window if its length is less than 24 s. If not, any window less than 16 s is counted as noise. With the noise windows determined, we interpolated seismic PSD 10 s out of each side of the noise window to fill the noise part.

Text S3. Earth structure response correction

In this study, to systematically analyze seismic PSDs from all stations, common precipitation windows for neighboring stations were first identified. Two stations are considered neighboring stations if their distance is within 1.5 km. Common precipitation windows were determined based on their average seismic PSD between 100 and 200 Hz (e.g. Figure 2d). Seismic PSDs were first smoothed by taking the average around ±15 s, and a noise level is defined as the root mean square of the smoothed seismic PSD before and after the precipitation event. We then find all windows with seismic PSD greater than three times the noise level and longer than 90 s. We also required these windows to have a maximum PSD higher than six times the noise level, and the average PSD within the window greater than 70% of the average PSD when the window has both sides extended by 2 min, to ensure that the window not only contains high amplitudes but also those high amplitudes are not for a trough between two large peaks. Windows with lengths over 20 min are divided into multiple 20-minute windows. Each window then has its two sides extended by 40 s and tapered to zero. The signal-to-noise ratio (*snr*) for each window is defined as the maximum PSD within the window divided by the noise level.

With these precipitation windows, the seismic PSD difference for station pairs (eq. 3) are measured. For each pair, we first calculated the cross-correlation between their seismic PSD time series (*psd*). If the maximum value of the cross-correlation (CC_{max}) appears within 3.5 min to the zero time, suggesting precipitation happens at similar times for the two events, we calculated their PSD difference by:

$$\log \frac{PSD_i}{PSD_k} = \log \frac{CC_{max}(psd_i, psd_k)}{CC_0(psd_k, psd_k)}, \tag{S10}$$

where CC_0 is the cross-correlation value at zero time, and i, k are indices for two stations. The quality of the cross-correlation is characterized by the correlation coefficient (cc) as:

$$cc = \frac{CC_{max}(psd_i, psd_k)}{\sqrt{CC_0(psd_i, psd_i) \times CC_0(psd_k, psd_k)}}. \tag{S11}$$

Then, we defined a weighting function as:

$$w(x,a,b) = \begin{cases} 0, & x \le a \\ 0.5 - 0.5\cos(\pi \dfrac{x-a}{b-a}), & a < x < b \\ 1, & x \ge b \end{cases}, \tag{S12}$$

and with these, the weight for each station pair PSD difference measurement is defined as:

$$\mathfrak{w}_{i,k} = w(cc, 0.55, 0.95) \times w(snr_i, 4, 10) \times w(snr_k, 4, 10) \times w(T, 0, 10), \tag{S13}$$

where T is the length of the window in min. Then, with the weight for each window, the overall PSD difference between the station pair ($r_{i,k}$) is obtained by weighted averaging measured $\log(PSD_i/PSD_k)$ of all windows, to eliminate source effects in eq. (3). In practice, after obtaining $r_{i,k}$ and the standard deviation ($std_{i,k}$) for those measurements, we eliminate those windows with measured $\log(PSD_i/PSD_k)$ not within 2.5 times the $std_{i,k}$ around the $r_{i,k}$, and this operation is performed iteratively until all windows are within this range or the number of left windows is less than 10. For following analyses, to obtain the relative Earth structure response, we used a weight $W_{i,k} = \sum_{windows} \mathfrak{w}_{i,k}$ to characterize the overall quality of measurements for each station pair.

The relative Earth structure response (R) with respect to a reference station is then calculated based on Newton's method (e.g. Galántai, 2000). In this study, the optimal Earth structure response for stations was found by minimizing the following cost function:

$$J(\mathbf{R}) = \sum_{i,k} W_{i,k} \frac{\left(\mathcal{R}_i - \mathcal{R}_k - r_{i,k}\right)^2}{2std_{i,k}^2}, \tag{S14}$$

where $\mathcal{R}_i$ stands for the log-scale relative structure response (logR_i), and is the i^{th} component of the vector **R**. Then, the m^{th} component of the gradient (**g**) of the cost function (with respect to $\mathcal{R}_m$) is expressed as:

$$g_m = \sum_{i,k} W_{i,k} \frac{\left(\mathcal{R}_i - \mathcal{R}_k - r_{i,k}\right)\left(\delta_{im} - \delta_{km}\right)}{std_{i,k}^2}, \tag{S15}$$

where δ here is the Kronecker delta. Then, the Hessian matrix (**H**), i.e. the gradient of **g**, has its (m^{th}, n^{th}) element as:

$$H_{mn} = \sum_{i,k} \frac{W_{i,k}}{std_{i,k}^2}\left(\delta_{im} - \delta_{km}\right)\left(\delta_{in} - \delta_{kn}\right). \tag{S16}$$

With the Hessian and gradient, based on Newton's method (Galántai, 2000), the optimization can be iteratively updated from the l^{th} to the $l+1^{\text{th}}$ iteration by:

$$\mathbf{R}_{l+1} = \mathbf{R}_l - \mathbf{H}_l^{-1}\mathbf{g}_l. \tag{S17}$$

However, because Hessian in this problem is explicit and not dependent on **R**, the cost function is quadratic, and for any assumed starting **R**, the same final optimal **R** can be achieved by updating eq. (S17) once, i.e., the problem does not require multiple iterations. Meanwhile, while obtaining the optimal relative Earth structure response **R** (Figure S1a) through eq. (S17), the uncertainty is also obtained as the covariance matrix for **R** is just the inverse of the Hessian matrix in eq. (S16) (Thacker, 1989), and the square roots of diagonal elements in the covariance matrix are thus standard deviations of the relative Earth structure response (σ) for each station (Figure S1b). Currently, station 340 (Figure S1) is set as the reference station because the summed standard deviation from all other stations is minimal.

Text S4. Obtaining seismic PSD at any location through spatial averaging

After obtaining seismic PSDs at different stations, and having their relative Earth structure responses removed, we used weighted spatial averaging to obtain the seismic PSD for any location within the study area. The weight for one precipitation event at a specific station is defined as:

$$\mathcal{W} = [1 - w(\sigma, 0.03, 0.08)] \times w(noise, 19.3, 20.2) \times [1 - w(d, 0.1, 1.7)], \quad \text{(S18)}$$

where w is the weighting function in eq. (S12); σ is the standard deviation for the log-scale relative Earth structure response $\mathcal{R}$; d is the distance from the station to the location of interest in km; and *noise* is the noise level we estimated for this precipitation event at the station. To estimate the noise level, we first obtained the $\log_{10}$ scale of the time series for the average seismic PSD between 100 and 200 Hz, which is then smoothed by taking the average around ±5 s. The noise level (*noise*) is defined by the root mean square of this smoothed time series at times before and after precipitation. Because the $\log_{10}$ of PSD is always negative, after taking the root mean square, the lower the *noise* value, the stronger the noise is. With the weight in eq. (S18), the time series after transformed into log-scale (*psdl*) at a random location is obtained by:

$$psdl = \frac{\sum_i \mathcal{W}_i \, psdl_i}{\sum_i \mathcal{W}_i}, \quad \text{(S19)}$$

where i is the index for the station. The total weight at the location $\sum_i \mathcal{W}_i$ is used to characterize the reliability of the averaging, and for maps shown in this study (e.g., Figure 4), only places with total weight higher than 1.5 are considered with a sufficient amount of data and analyzed.

Text S5. Converting seismic PSD to precipitation rate

To convert seismic PSDs for individual sub-events (Figure 3) to precipitation rate based on eq. (2), first we rewrite the relationship in log-scale as:

$$\log PR = \log PSD - \log E - \log 2\rho_w S\,. \tag{S20}$$

Here, the last part of the right-hand side is a constant among stations after removing relative Earth structure responses, and if E depends on the precipitation rate, the relationship is characterized by:

$$\log PR = p \log PSD + q\,, \tag{S21}$$

where p and q are slope and intercept of a linear model to be solved. These two values were obtained through the ordinary least-squares method, and all-time steps with both smoothed precipitation rates (e.g., Figure 3c) over 1 mm hr^{-1} and smoothed seismic PSD (e.g., Figure 3b) over tripled mean noise level among neighboring stations were used in the linear regression. The noise level was defined when forming the weighting function (eq. S18) for spatial averaging.

To obtain the overall linear relationship in Figure 3e, the same relationship in eq. (S21) and the ordinary least-square method was applied. However, since different sub-events have different durations, to weight them equally, we used the bootstrap method. At each iteration, 150 time points were randomly picked from each sub-event (except the two abnormal ones, the first sub-event on 26 April 2016 and the event on 18 April 2016, shown as dashed lines in Figure 3e), and the seismic PSD was fitted to the precipitation rate for these times using the ordinary least-square method to obtain p and q in eq. (S21). We ran 3,000 iterations in total, and the average p and q were used to represent the overall relationship in Figure 3e. The 95% prediction interval that characterizes the spread of the data (Figure 3e) was also obtained alongside by averaging prediction intervals obtained at those iterations. This relatively large interval would likely to be the combined effect of various raindrop kinetic energies for different sub-events, and the time-lag between seismic PSDs and rain gauge precipitation rates. The time-lag is partly because no seismic station co-locates with the rain gauge, and the spatial averaged seismic PSD is only an approximation for the rain gauge location. It is also partly because the integration time for rain gauge (tipping time) would lag the time the rain was first collected, which makes the seismic PSD often lead the rain gauge precipitation (Figures 3 & S2).

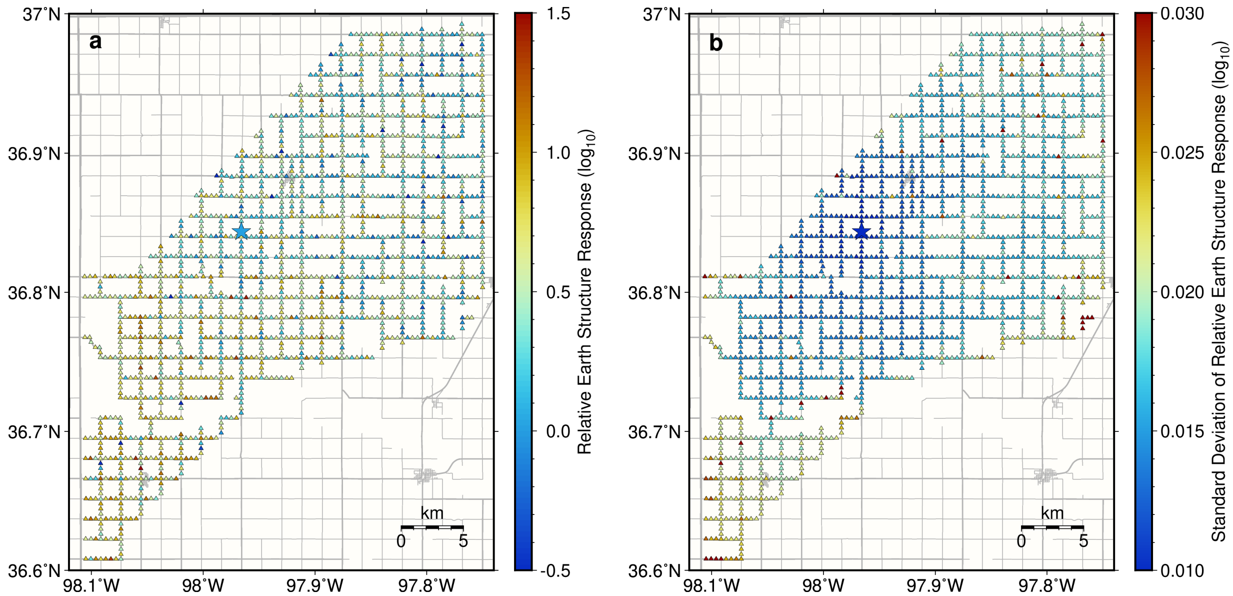

Figure S1. Normalization of Earth structure responses. (a) The same as Figure 1, relative site responses for different stations with respect to the reference Station: 340 (star). (b) The standard deviation for the obtained relative site response in (a).

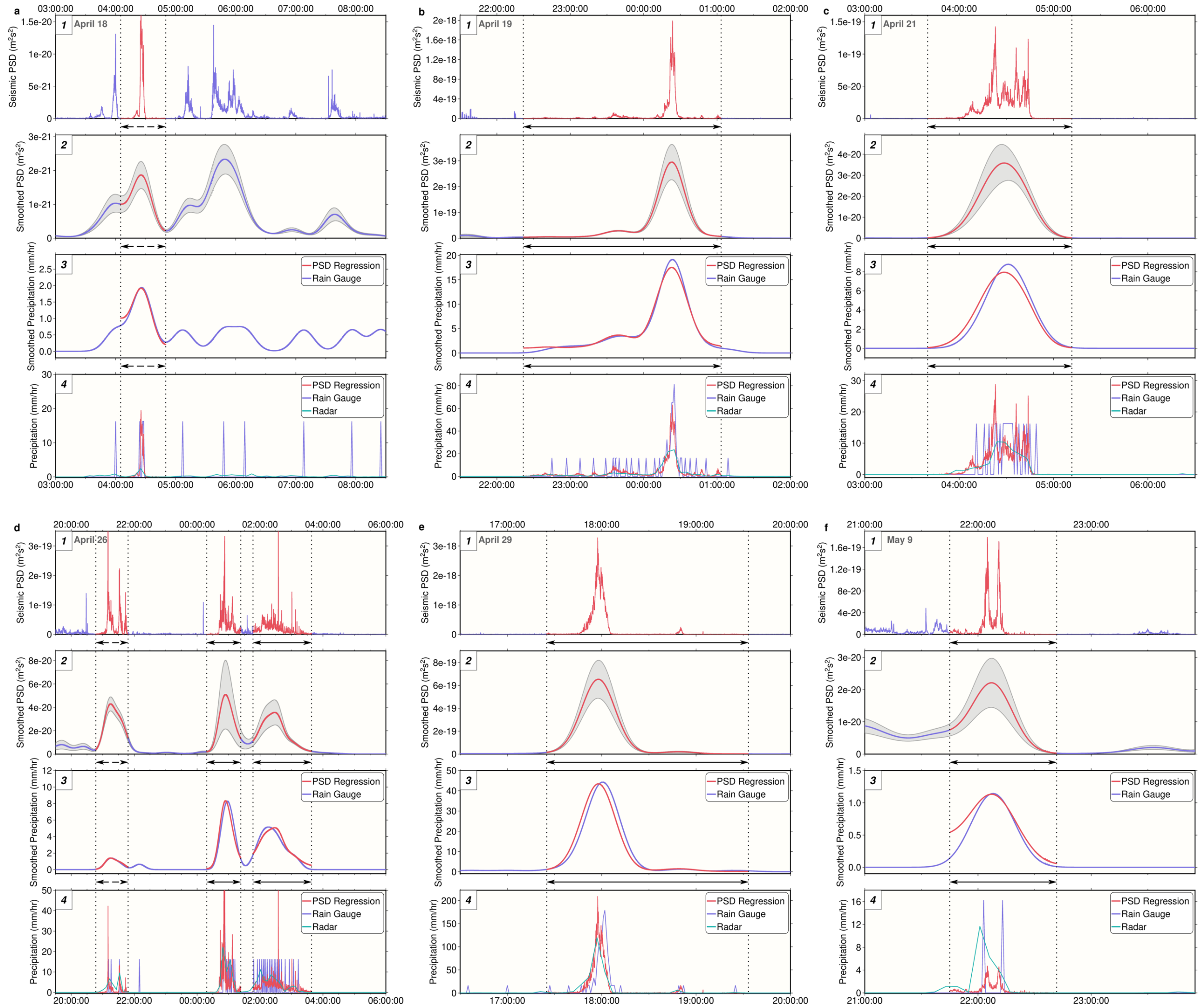

Figure S2. Seismic precipitation measurements in comparison with rain gauge. (a)-(f) correspond to events starting at the date indicated in the top left corner of their first sub-panel. (f) is for the second event on 9 May 2016. Events starting on 8 May 2016, and the first event on 9 May 2016 did not pass the rain gauge (Movie S7, Movie S8). Four sub-panels in each panel correspond to the Figure 3a-d.

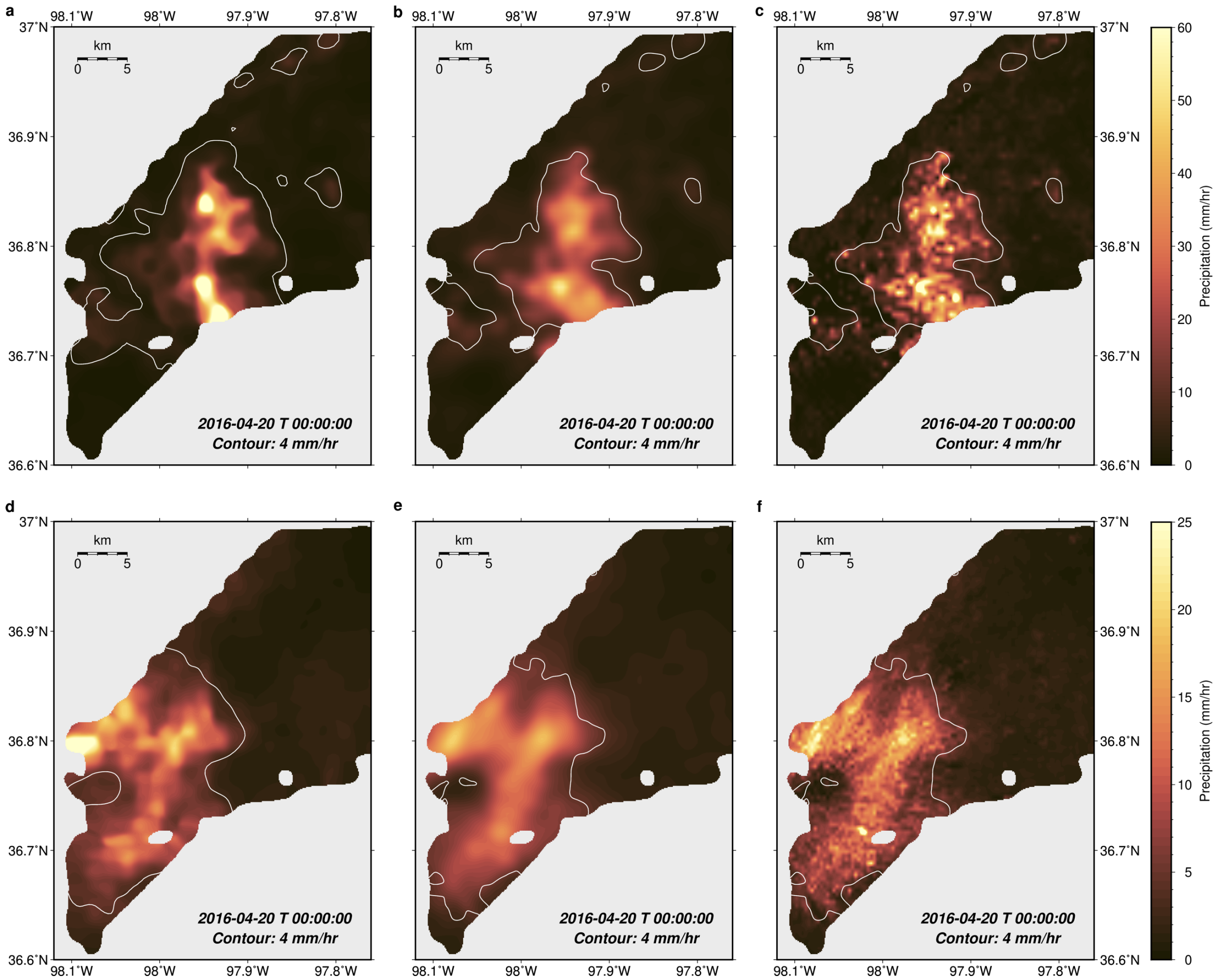

Figure S3 Precipitation spatial distribution from seismic array and weather radar. (a)-(c) Instantaneous precipitation rate at 00:00:00 UTC 20 April 2016 from converted seismic PSD (a: using the relationship in Figure 3e); weather radar (b); weather radar without smoothing (c). White lines in (a) for the contour of 4 mm hr^{-1} in (b), and white lines in (b) and (c) for the contour of 4 mm hr^{-1} in (a). (d)-(f) Similar to (a)-(c), but for the averaged precipitation rate over one hour before the time, which is bias corrected with respect to the rain gauge for radar. Though without smoothing (c and f), the radar seems to provide a very high spatial resolution – those images are dominated by large oscillatory variations over short distances, and the unsmoothed radar precipitation region is still broader than the one from seismic array (a versus c). Gray areas are places with insufficient amount of data (criteria in Text S4 in Supporting Information S1).

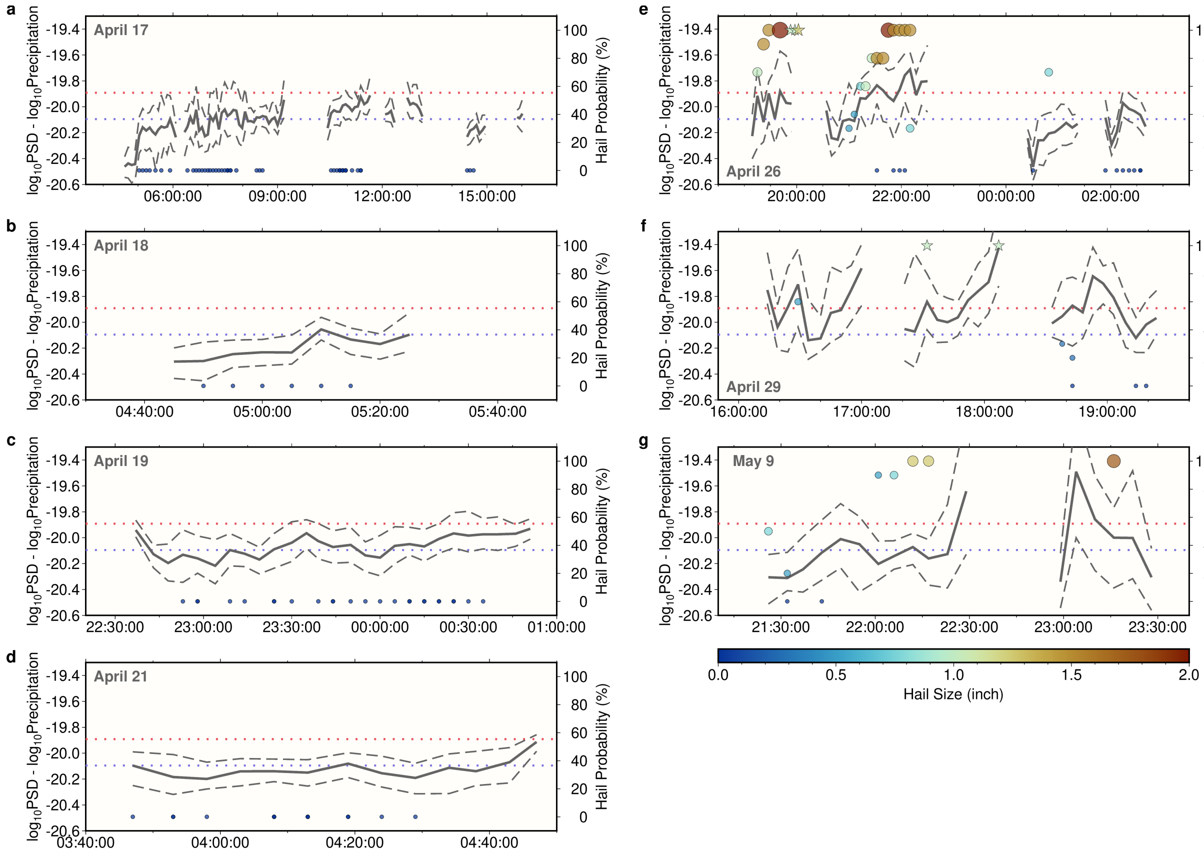

Figure S4. The relationship between seismic power spectral density and potential hailfall. (a)-(g). Seven precipitation events with hail parameters provided by the radar (the same set of events as in Figures 3 & S3, with starting dates labelled at top left corners). Gray solid/dashed lines and dotted lines have the same meaning as in Figure 5b. Circles and stars have the same meaning as in Figure 5a.

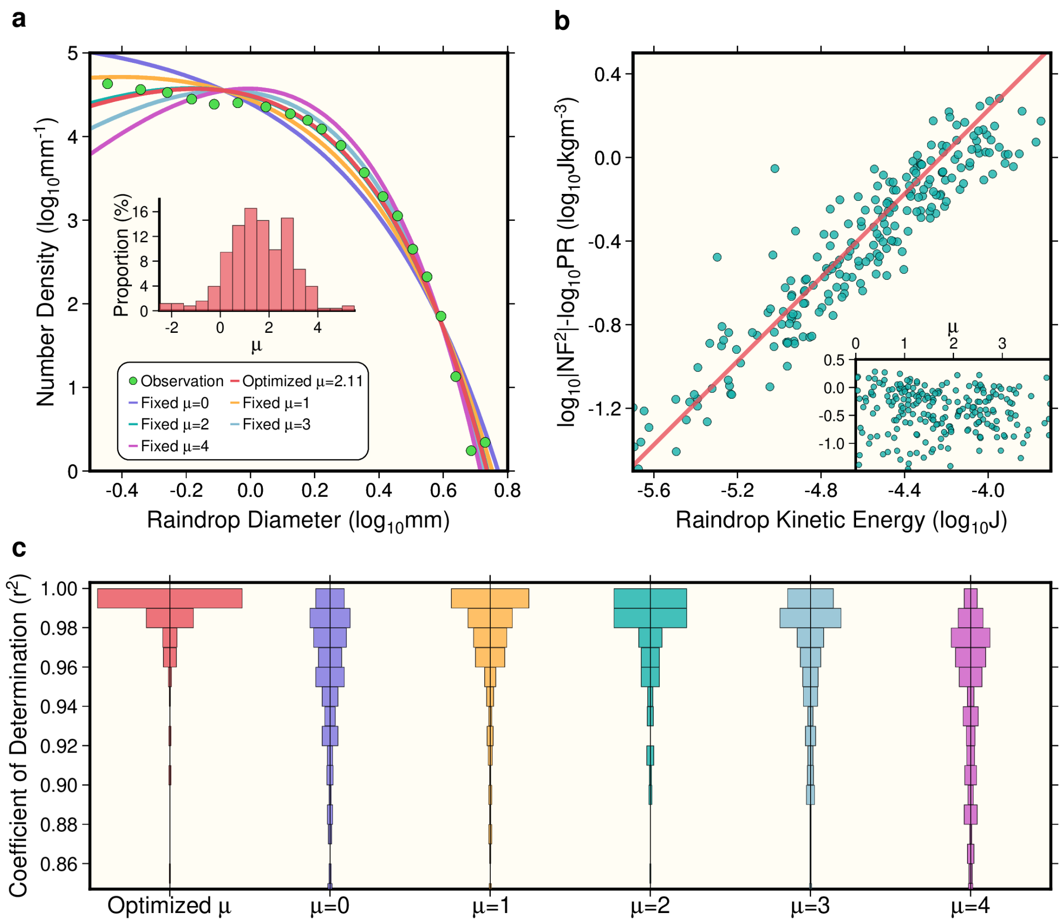

Figure S5. The influence of raindrop size distribution. (a) The raindrop size distribution from a disdrometer located ~30 km away from the study region on 4 April 2019. Dots are total counts of raindrops per diameter at that day in log-scale. Lines are fitted distribution based on eq. (S1). For the red line, μ, N_0, and D_0 are fitted together. For other lines, we prescribed μ from 0 to 4 and only solved N_0 and D_0. The histogram in **a** shows the distribution of fitted μ for days between April 2016 and November 2021 with accumulated rainfall greater than 2 mm (together 257 days). (b) The relationship between raindrop kinetic energy (E) and the PSD-PR difference. Each dot corresponds to one day, and both axes are calculated based on provided N(D), $m(D)$, $v(D)$ from the disdrometer. The line, instead of based on disdrometer records, shows the theoretical relationship when μ is fixed at 2 (eq. S8; y-axis: $2\rho_w[\Gamma(\mu+8)\,\Gamma(\mu+1)]/[\,\Gamma(\mu+5)\,\Gamma(\mu+4)]E$). The inset plot is based on the same set of data, but while y-axis is the same as the main plot, the x-axis is for fitted μ. This panel shows a much stronger relationship between the PSD-PR difference and the kinetic energy than that between the PSD-PR difference and μ. (c) The distribution of coefficient of determination (commonly known as r^2) for the fitting of all the days. Six histograms are for cases where we fit μ, N_0, and D_0 together (optimized μ), or fix μ at different values and only solve N_0 and D_0. It is shown though solving all three parameter results in the highest r^2, fixing μ at reasonable values, such as 2, does not degrade the overall result much.

Event Number	Starting Date (Year: 2016)	Approximate Event Time Frame (UTC)	Dominant Storm Type
1	April 17	02:00:00-20:00:00	MCS* with trailing stratiform rain region
2	April 18	01:00:00-09:00:00	Stratiform rain
3	April 19	20:00:00-02:00:00	North end of an MCS
4	April 21	03:00:00-06:00:00	Decaying MCS
5	April 26	19:00:00-04:00:00	Supercells transitioning toward MCS
6	April 29	15:00:00-20:00:00	Potential supercells/isolated cells
7	May 8	11:00:00-20:00:00	Scattered cells
8	May 9	02:00:00-04:00:00	Decaying supercells
9	May 9	21:00:00-00:00:00	Potential supercells/isolated cells

*MCS: Mesoscale Convective System

Table S1. A summary of the nine observed precipitation events. The dominant storm type was manually determined from archived weather radar data that was viewed at the following website: https://www2.mmm.ucar.edu/imagearchive/.

Symbols for the Physical Meaning of Seismic Precipitation Signals		Symbols for Data Processing	
PSD	Power spectrum density (eq. 2)	R	Relative Earth structure response (Section 2.2)
F	Impact force (eq. 1)	CC_0	Cross-correlation value at zero time (eq. S8)
G	Displacement Green's function (eq. 1)	CC_{max}	Maximum cross-correlation value (eq. S8)
PR	Precipitation rate (eq. 2)	cc	Correlation coefficient (eq. S11)
E	Raindrop kinetic energy (eq. 2)	psd	The time series of PSD at 100-200 Hz (eq. S10)
S	Combined Earth Structure Response (eq. 2)	snr	Precipitation window signal-to-noise ratio (eq. S13)
N	Number of raindrops per area per time (eq. 2)	T	Precipitation window length (eq. S13)
u	Seismic displacement (eq. 1)	w	Weighting function (eq. S12)
f	Seismic frequency (eq. 1)	$\mathfrak{w}$	Weight for station pair PSD difference measurements (eq. S13)
r	Distance between raindrop impact and seismic station (eq. 1)	W	Summed weight for each station pair (eq. S14)
m	Raindrop mass (eq. 1)	$r_{i,k}$	Overall measured PSD difference between stations i and k (eq. S14)
v	Raindrop fall speed (eq. 1)	$std_{i,k}$	Standard deviation for measured $\log(PSD_i/PSD_k)$ (eq. S14)
t	Time (eq. 1)	$\mathcal{R}$	Log-scale R (eq. S14)
t_j	Time for impact j (eq. 1)	J	Cost function (eq. S14)
ρ_w	Raindrop density (eq. 2)	$\mathbf{R}$	The vector of (eq. S14)
ρ_a	Air density (eq. S2)	$\mathbf{g}$	Gradient of the cost function (eq. S15)
$N(D)$	Number of raindrops per area per time per diameter (eq. S1)	$\mathbf{H}$	Hessian of the cost function (eq. S16)
N_0	Characteristic number of raindrops per area per time (eq. S1)	$\mathcal{W}$	Weight for spatial averaging (eq. S18)
D	Raindrop diameter (eq. S1)	σ	Standard deviation of $\mathcal{R}$ (eq. S18)
D_0	Characteristic raindrop diameter (eq. S1)	$noise$	Noise level for precipitation event (eq. S18)
μ	Shape parameter for $N(D)$ (eq. S1)	d	Distance from station to the location for spatial averaging (eq. S18)
g	Gravitational acceleration (eq. S2)	$psdl$	Log-scale psd (eq. S19)
i, k	Indices for stations	p, q	Free parameters for linear regression (eq. S21)
j	Index for impact	m, n	Indices for $\mathbf{R}$, $\mathbf{g}$, and $\mathbf{H}$

Table S2. The summary of symbols used in this study. Symbols appeared in both the main text and Supporting Information S1 are included. Where these symbols first appear in equations are also indicated.

Movie S1. Precipitation spatial evolution for the event on 17 April 2016. Top row from left to right shows the log-scale seismic PSD (as in Figure 4a); seismic converted precipitation rate with the relationship in Figure 3e (as in Figure S3a); seismic converted one-hour precipitation accumulation (as in Figure S3b); the current time (red line) and the satellite precipitation rate for the study area (blue line). The bottom row from left to right shows the log-scale radar instantaneous precipitation rate (as in Figure 4b); radar instantaneous precipitation rate (as in Figure S3d); radar one-hour precipitation accumulation without gauge-radar bias (as in Figure S3e); the difference between seismic PSD and radar instantaneous precipitation rate (as in Figure 4c). For the first three columns, white lines in the top row show contour derived in the bottom row at the value indicated in the panel, and vice versa. Contour levels for seismic PSD are converted to precipitation rate using the formula in Figure 3e. Radar images are updated more slowly due to lower time resolution.

Movie S2. Precipitation spatial evolution for the event on 18 April 2016. Similar to Movie S1, but for a different event.

Movie S3. Precipitation spatial evolution for the event on 19 April 2016. Similar to Movie S1, but for a different event.

Movie S4. Precipitation spatial evolution for the event on 21 April 2016. Similar to Movie S1, but for a different event.

Movie S5. Precipitation spatial evolution for the event on 26 April 2016. Similar to Movie S1, but for a different event.

Movie S6. Precipitation spatial evolution for the event on 29 April 2016. Similar to Movie S1, but for a different event.

Movie S7. Precipitation spatial evolution for the event on 08 May 2016. Similar to Movie S1, but for a different event.

Movie S8. Precipitation spatial evolution for the first event on 09 May 2016. Similar to Movie S1, but for a different event.

Movie S9. Precipitation spatial evolution for the second event on 09 May 2016. Similar to Movie S1, but for a different event.